Deep, noninvasive imaging and surgical guidance of submillimeter tumors using targeted M13-stabilized single-walled carbon nanotubes

Debadyuti Ghosh[a,b,1,2], Alexander F. Bagley[a,c,d,1], Young Jeong Na[e], Michael J. Birrer[e], Sangeeta N. Bhatia[a,f,g,h,i,3,4], and Angela M. Belcher[a,b,j,3,4]

[a]Koch Institute for Integrative Cancer Research, Departments of [b]Materials Science and Engineering, [g]Electrical Engineering and Computer Science, and [j]Biological Engineering, [f]Harvard–MIT Division of Health Sciences and Technology, [h]Institute for Medical Engineering and Science, and [i]Howard Hughes Medical Institute, Massachusetts Institute of Technology, Cambridge, MA 02139; [c]Biophysics Program, Harvard University, Boston, MA 02115; [d]MD–PhD Program, Harvard Medical School, Boston, MA 02115; and [e]Department of Medicine, Massachusetts General Hospital, Harvard Medical School, Boston, MA 02114

Highly sensitive detection of small, deep tumors for early diagnosis and surgical interventions remains a challenge for conventional imaging modalities. Second-window near-infrared light (NIR2, 950–1,400 nm) is promising for in vivo fluorescence imaging due to deep tissue penetration and low tissue autofluorescence. With their intrinsic fluorescence in the NIR2 regime and lack of photobleaching, single-walled carbon nanotubes (SWNTs) are potentially attractive contrast agents to detect tumors. Here, targeted M13 virus-stabilized SWNTs are used to visualize deep, disseminated tumors in vivo. This targeted nanoprobe, which uses M13 to stably display both tumor-targeting peptides and an SWNT imaging probe, demonstrates excellent tumor-to-background uptake and exhibits higher signal-to-noise performance compared with visible and near-infrared (NIR1) dyes for delineating tumor nodules. Detection and excision of tumors by a gynecological surgeon improved with SWNT image guidance and led to the identification of submillimeter tumors. Collectively, these findings demonstrate the promise of targeted SWNT nanoprobes for noninvasive disease monitoring and guided surgery.

cancer imaging | fluorescence-guided surgery | M13 bacteriophage

In clinical oncology, in vivo fluorescence imaging has emerged as a valuable tool for improving diagnosis, staging tumors, monitoring response to therapy, and detecting recurrent or residual disease. Compared with existing imaging modalities, fluorescence imaging offers a low-cost, portable, and safe alternative (i.e., nonionizing radiation), with key advantages including real-time imaging, superior resolution, and high specificity for small tumor nodules during diagnostic and intraoperative surgical procedures (1, 2). Although efforts have focused on using visible and short near-infrared (NIR1, 650–900 nm) wavelength fluorescent dyes as contrast agents for delineating tumor margins in both preclinical cancer models (2, 3) and human patients (4), these agents are suboptimal for noninvasive, reflectance-based imaging due to limited penetration depth (3–5 mm) and high tissue autofluorescence. During intraoperative surgery, these dyes may additionally undergo photobleaching, thereby reducing the ability of the surgeon to readily locate and resect tumors. Alternative approaches to specifically permit noninvasive imaging and limited photobleaching would be highly desirable for diagnostic and surgical applications.

Single-walled carbon nanotubes (SWNTs) hold great promise as fluorescence imaging agents due to the large interband difference between their excitation and emission wavelengths, resulting in minimal spectral overlap and tissue autofluorescence. In particular, the low tissue autofluorescence observed with SWNTs greatly enhances target-to-background ratios (TBRs) necessary for improved detection of small tumor nodules in confined anatomic regions. SWNT emission at longer wavelengths in the near-infrared second window (NIR2, 950–1,400 nm) results in less optical scattering and deeper tissue penetration compared with shorter wavelength visible and NIR1 imaging agents. Simulations (5) and experimental results (6) suggest the greatest tissue penetration depth is achieved in the NIR2 regime, which further supports the potential value for use of SWNTs for biological imaging applications. Additionally, unlike visible and near-infrared dyes, well-functionalized SWNTs are less susceptible to photobleaching or quenching effects (7), which make them attractive for continuous, long-term imaging required during many surgical procedures. Previously, we have demonstrated that M13 bacteriophage-stabilized SWNTs can target s.c. prostate tumors in preclinical models for fluorescence imaging in the second optical window (8). SWNTs have also been used for vascular and deep tissue fluorescence imaging (9). Importantly, M13 serves as a scaffold to couple both targeting and imaging moieties while allowing them to retain their functionalities (10); in comparison,

Significance

Early detection of cancer positively impacts diagnosis and treatment, ultimately improving patient survival. Using fluorescence imaging offers the promise of safe, noninvasive detection with excellent resolution and guides surgical removal of tumors to improve patient outcomes. However, the success of current optical probes is limited due to high background from tissue autofluorescence, poor penetration depth, and inherently low signal stability. Here, we engineered M13 bacteriophage to stabilize single-walled carbon nanotubes for selective, targeted imaging of ovarian tumors. These nanoprobes fluoresce at longer near-infrared wavelengths than current probes, thereby improving noninvasive detection of small, deep tumors and guidance for surgical removal of submillimeter tumors. This material-based approach may be attractive to guide surgical interventions where deep tissue molecular imaging is informative.

more prevalent nanoparticle systems directly conjugated with targeting ligands may require optimization of ligand density for effective targeting (11, 12). Also, the identification of tissue-targeting peptides via phage display has been valuable for enhancing nanoparticle trafficking in vivo (13, 14). However, to date, there has been no report of an affinity-targeted, fluorescence imaging agent capable of noninvasive imaging and guiding diagnosis for surgical resection.

Here we report an M13-stabilized SWNT probe that selectively targets Secreted Protein, Acidic and Rich in Cysteines (SPARC)-expressing tumor nodules in an orthotopic mouse model of human ovarian cancer. Ovarian cancer remains a major health care problem for women. Annually, 225,000 women worldwide are diagnosed with epithelial ovarian cancer (EOC) and ~140,000 women die as a result (15). Although women with early-stage ovarian cancer [International Federation of Gynecology and Obstetrics (FIGO) stage I/II] can be cured, advanced-stage ovarian cancer (FIGO III/IV) remains considerably more difficult to treat. Unfortunately, 80% of women with EOC have metastatic disease at the time of diagnosis, and many undergo a treatment regimen of surgery and chemotherapy. Our study focused on ovarian cancer because clinical evidence indicates that optimal surgery can significantly prolong the median overall survival of patients as well as reduce disease morbidity (16). Using the NIR2 emission of these fluorescence probes, we determine the detection limit of labeled tumors and their TBRs. We demonstrate that this SWNT-based probe detects tumors that were missed when either visible or NIR1 dyes were used, thereby aiding the discovery of smaller tumors during surgery. Collectively, our results highlight the potential for affinity-targeted NIR2 fluorescence probes to monitor disease processes such as cancer with enhanced sensitivity compared with current state-of-the-art optical probes.

Results

Characterization of the M13-Stabilized SWNT Probe.

The imaging probe [SPARC binding peptide (SBP)–M13–SWNT] consists of three fundamental components: the SBP, M13 virus, and SWNTs (Fig. 1A). The filamentous M13 virus (6 nm diameter, 880 nm length) is genetically modifiable such that peptides can be incorporated for display on the various coat proteins of the virus. By displaying peptides with varying affinities to materials or biomolecules through an iterative panning and selective enrichment process, M13 is well suited for diverse applications including epitope mapping (17), ligand discovery against cells and tissues (18), and binding and nucleation of materials (19, 20). The modularity of M13 can be further exploited to target various biomarkers in cancers, highlighting its attractiveness as a multifunctional probe. Previously, we used phage display to identify a peptide along the p8 major coat protein of M13 that binds and stabilizes SWNTs (20), while retaining the optical and electronic properties of the nanotubes. Because M13 can be genetically engineered to display 100% of fusion peptides, we further engineered the p3 minor coat protein to display five copies of a targeting peptide that binds SPARC (21). SPARC is a matricellular protein highly expressed in certain subtypes of breast, prostate, and ovarian cancer. SPARC overexpression has been shown to enhance ovarian cancer cell proliferation, invasion, and metastasis. High levels of SPARC expression have been associated with late stages of ovarian carcinoma and correlated with poor clinical prognosis (22), suggesting its relevance as a clinical biomarker. Collectively, these traits have been taken into account in the design of this genetically engineered NIR2 probe in order to enable the localization, detection, and surgical excision of ovarian tumors, as outlined in the schematic presented in Fig. 1A.

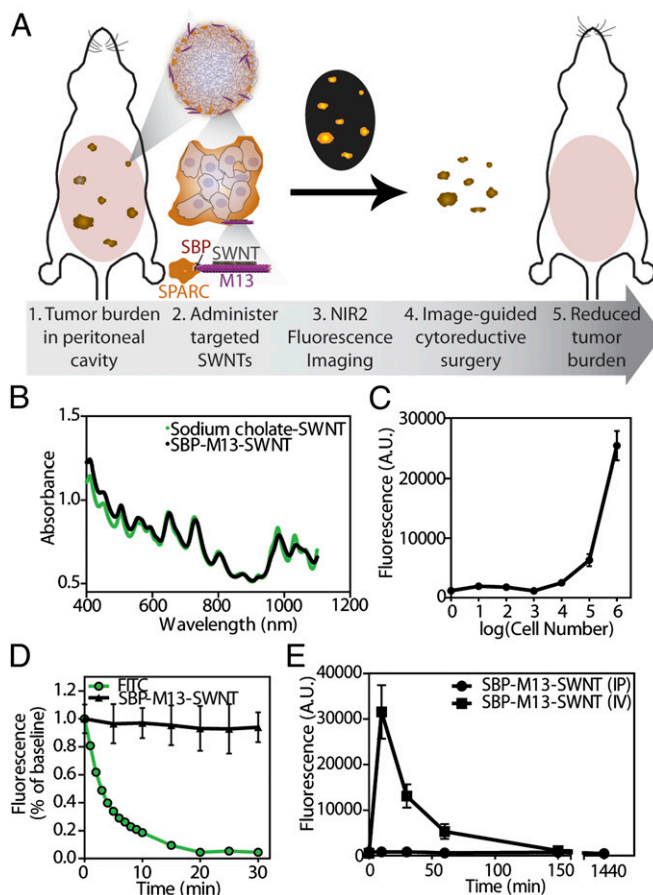To ensure that our probe retained its functionality following synthesis, we examined the optical properties of SBP–M13–

Fig. 1. Characterization of tumor-targeting SBP–M13–SWNT probe. (A) Schematic illustrating association with ovarian tumor nodules for noninvasive detection by NIR2 fluorescence and surgical excision. (B) Absorbance spectra of SWNTs in sodium cholate and as SBP–M13–SWNT probe. (C) In vitro sensitivity of SBP–M13–SWNT fluorescence in ovarian cancer cell culture. n = 3 per group. Error bars represent SE. (D) Photobleaching fluorescence decay of FITC and SBP–M13–SWNTs under continuous excitation. Error bars represent SD. (E) Pharmacokinetic circulation study of SBP–M13–SWNT administered i.v. (IV) and intraperitoneally (IP). n = 3 per timepoint. Errors bars represent SE.

SWNTs. Compared with unmodified SWNTs dispersed in sodium cholate, complexed SBP–M13–SWNTs exhibited similar optical absorbance that was consistent across multiple batches (Fig. 1B and *SI Appendix*, Fig. S1). Previously, photoluminescence (fluorescence) mapping of the excitation and emission wavelengths of SBP–M13–SWNTs suggests M13-stabilized SWNTs retain their fluorescent properties; nondispersed, aggregating, or bundled SWNTs would quench and not fluoresce and thus not appear in the fluorescence mapping (8).

To establish their use for in vivo applications, we validated the stability of SBP–M13–SWNTs in blood and ascites and at different pH values by measuring the fluorescence over 24 h using a custom-built small-animal NIR2 fluorescence imager (8). SBP–M13–SWNTs retain fluorescence at various dilutions in the blood and ascites fluid from the peritoneal cavity (*SI Appendix*, Figs. S2 and S3, respectively), and we did not observe quenching of the probe. Previous reports indicate that exposed SWNTs in solution will adsorb serum proteins on their sidewall and subsequently lose fluorescence (8, 23). Here, we observe no loss of fluorescence intensity, indicating the probes are well solubilized by M13 and highly stable for in vivo imaging applications. In addition, the probe is fluorescently stable across a broad pH range, from 4.5 to 8.5 (*SI Appendix*, Fig. S4), suggesting the

probes will be stable in the vascular and lymphatic systems and the peritoneal cavity and for cellular uptake. We also confirmed the targeted probes are not acutely cytotoxic to primary human endothelial cells and ovarian carcinoma cell line 8 (OVCAR8) (*SI Appendix*, Figs. S5 and S6, respectively), which builds upon previous studies on cell-type dependence of nanomaterial toxicity (24) and underscores their potential for in vivo imaging applications.

We next examined the sensitivity of the probe in terms of its capacity to target OVCAR8 ovarian cancer cells in vitro. Serial 10-fold dilutions of OVCAR8 cells were incubated with SBP–M13–SWNT for 24 h, and cell lysates were collected. Measuring the fluorescence intensity of the SBP–M13–SWNT incubated cells, we observed that as few as ~10,000 cells incubated with SBP–M13–SWNT exceeded the minimum level of detection (Fig. 1C).

To test SBP–M13–SWNTs for risk of photobleaching, we exposed them to an 808-nm laser for a continuous, 30-min period and measured fluorescence intensity in 5-min intervals up to 30 min postirradiation. No appreciable loss of fluorescence of SBP–M13–SWNTs was observed during this period. However, the intensity of fluorescein isothiocyanate (FITC), a fluorescein derivative that has been used to molecularly image and guide intraoperative resection of ovarian tumors in humans (4), exponentially decreased in response to the same light exposure kinetics (Fig. 1D). The observations that SWNTs do not photobleach and maintain their optical properties illustrate their potential to assist surgeons in visualizing tumors during resection.

Another potential advantage of SWNT-based imaging compared with FITC-based imaging is the potential to detect tumors located at greater depths in the body. To investigate the depth of detection that can be achieved with our probe, we harvested ovarian tumors that had been treated with SBP–M13–SWNTs and imaged the small tumor fragments (~1-mm diameter) at various depths within a tissue "phantom" construct, which mimics the optical properties of human tissue. Using our NIR2 fluorescence reflectance imaging system (8), we could detect SWNT-containing tumors to depths as great as 9.7–18.2 mm (*SI Appendix*, Fig. S7). To our knowledge, this is the best reported quantifiable tumor depth using reflectance imaging, relative to previously reported values (3). By permitting deeper imaging, SBP–M13–SWNT therefore offers the potential for noninvasive detection before surgery and improved resection of tumors during surgery.

In Vivo Characterization of the SBP–M13–SWNT Probe. Having demonstrated in vitro stability and fluorescence of SBP–M13–SWNTs, we next characterized their in vivo properties in an orthotopic model of ovarian cancer. The OVCAR8 human cell line was used to create the orthotopic model, as it overexpresses SPARC, as confirmed by ONCOMINE (25) analysis and immunohistochemistry (*SI Appendix*, Fig. S8). To compare routes of administration, tumor-bearing animals were injected intraperitoneally or i.v., and the circulating probe concentration was monitored via SWNT fluorescence in the blood. The i.v.-administered SBP–M13–SWNTs reached a peak concentration in the circulation ~10 min after injection, and circulating levels became negligible after 150 min (Fig. 1E). Notably, SBP–M13–SWNTs injected intraperitoneally led to negligible elevations in blood-borne SWNT fluorescence for at least 24 h, suggesting that the majority of SBP–M13–SWNTs remain in the peritoneum postinjection (Fig. 1E). This finding was verified by the observation that, following a transient increase in NIR2 fluorescence in the peritoneum, the overall intensity in this location stabilizes for periods up to 24 h following injection (Fig. 2 A and B). Lastly, we studied the biodistribution of SBP–M13–SWNTs administered into the peritoneal cavity of tumored mice (*SI Appendix*, Fig. S9). The accumulation of SBP–M13–SWNTs was greatest in tumors at days 1 and 7 postinjection, with additional signal observed in
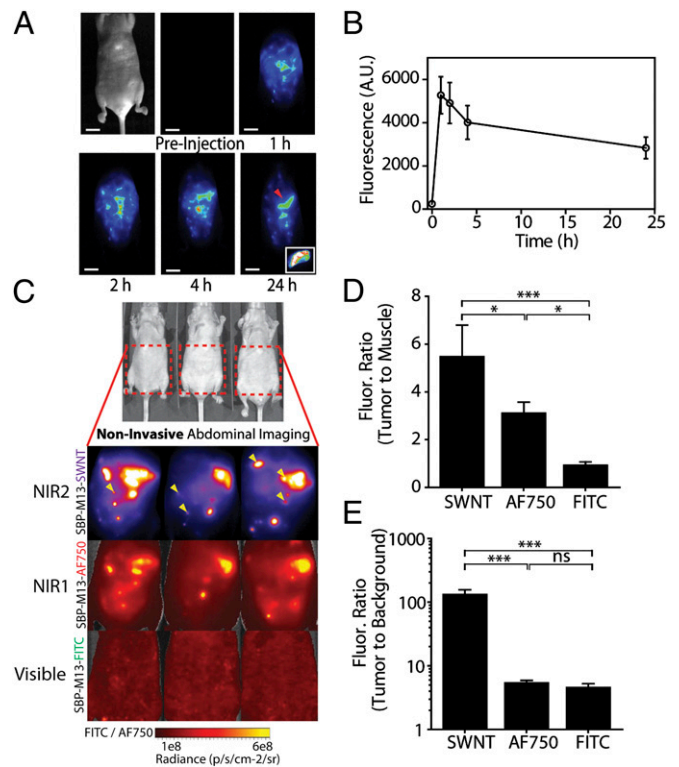

Fig. 2. Noninvasive tumor imaging with SBP–M13–SWNTs. (*A*) Representative whole-abdomen NIR2 imaging series following i.p. administration of SBP–M13–SWNTs. (*Inset*) Surgically excised tumor nodule (denoted by red arrow) observed 24 h postinjection of SBP–M13–SWNTs. (*B*) NIR2 fluorescence intensity in the abdomen of tumor-bearing animals following IP administration of SBP–M13–SWNTs up to 24 h postinjection ($n = 6$; error bars represent SE). (*C*) Noninvasive imaging of ovarian tumors using SBP–M13 conjugated to SWNTs (NIR2), AlexaFluor750 (NIR1), and FITC (Visible) (top to bottom). Arrows in the SWNT panel denote nodules visible only by SWNTs ($n = 3$ animals). (*D* and *E*) Tumor-to-muscle ratio and TBR from noninvasive images obtained with SWNTs, AF750, and FITC ($n = 3$ per group; ***$P < 0.001$; *$P < 0.05$; one-way ANOVA and Tukey posttests). Error bars, s.d. [Scale bar, 1 cm (*A*).]

liver, spleen, kidney, and peritoneum in the vicinity of the injection site. At day 7 postinjection, the lowest signals observed were in heart and lung tissue, supporting limited systemic exposure of SBP–M13–SWNT after i.p. administration. Importantly, analysis of serum from tumor-bearing animals following the administration of SBP–M13–SWNTs into the peritoneal cavity revealed no evidence of systemic hepatic, renal, metabolic, or hematologic acute toxicities within the first week following administration (*SI Appendix*, Fig. S10).

Improved Signal-to-Noise Performance in Vivo Using SBP–M13–SWNT in the NIR2 Wavelength Regime. Signal-to-noise behavior is a critical parameter for sensitive detection of tumors. To directly compare the signal-to-noise ratios between SWNTs and dyes in the NIR1 or visible regimes, SBP–M13 viruses were either complexed to SWNTs or conjugated with AlexaFluor750 dye (SBP–M13–AF750) or FITC (SBP–M13–FITC). Probes were then combined and added in fivefold excess of their minimum detection limits to mice bearing disseminated tumors. Noninvasive images were acquired through the fully intact skin of tumor-bearing animals (Fig. 2C), and fluorescence intensities from tumors in the peritoneal cavity, muscle, and background were determined. The tumor-to-muscle ratio of SBP–M13–SWNTs was 5.5 ± 1.2 (mean $\pm$ SD), which was significantly higher than ratios calculated for SBP–M13–AF750 (3.1 ± 0.42) and SBP–M13–FITC (0.96 ± 0.10) (Fig. 2D). The TBR (i.e., intensity of tumor to image

background) achieved using SBP–M13–SWNTs was 134.9 ± 21.0, which was a 24- and 28-fold improvement over SBP–M13–AF750 and SBP–M13–FITC, respectively (Fig. 2E). Importantly, as highlighted by the arrows in Fig. 2C, tumor nodules not observed in the visible and NIR1 channels were detectable in the NIR2 regime with SBP–M13–SWNTs, which highlights the sensitivity of the SWNT probe and imaging system.

Selective and Affinity Targeting of SBP–M13–SWNT to Ovarian Tumors in Vivo. Because many tumor nodules are implanted on the surfaces of peritoneal organs in this model, we also computed organ-specific TBRs for tumor nodules on the liver, intestine, and spleen. Representative photographs of organs containing tumor implants on their surface with their corresponding NIR2 fluorescent images are shown in Fig. 3A. The TBRs (i.e., ratio of surface tumor nodule fluorescence relative to that observed in its underlying organ) calculated for the liver, intestine, and spleen were 4.6, 8.0, and 3.1, respectively (Fig. 3B), highlighting the
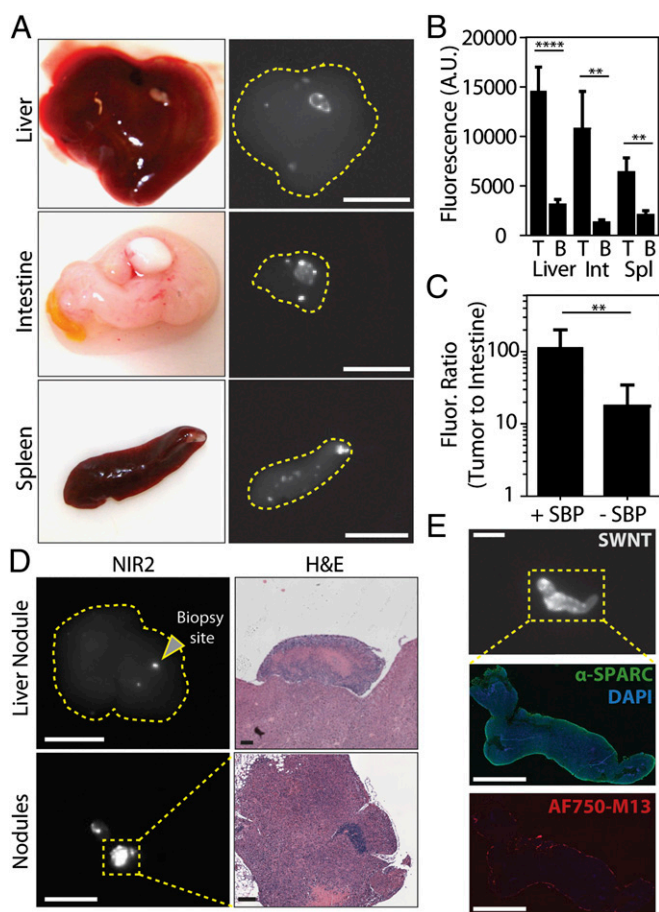

Fig. 3. Specificity of SBP–M13–SWNTs for OVCAR8 tumor nodules in the abdominal cavity. (A) Photographs and NIR2 fluorescence (10–50-ms exposure) of tumor nodules implanted on several peritoneal organs. (B) Quantification of nodule and organ-specific background for nodules present on the liver, intestine, and spleen (n = 8–11 nodules per organ; **P < 0.01; ****P < 0.0001; two-tailed t tests). (C) Tumor-to-intestine ratio for targeted and untargeted M13–SWNT probes. Intestinal tissue used for background intensity (+SBP, n = 6; –SBP, n = 13; **P < 0.01; two-tailed t test). (D) Representative NIR2 fluorescence and H&E staining of a positive nodule revealing characteristic tumor histology. (E) Immunofluorescence staining reveals colocalization of M13–SBP–SWNTs conjugated to AlexaFluor750 dye with SPARC expression in an NIR2-positive nodule. [Scale bars, 10 mm (A), 10 mm (D, NIR2), 250 µm (D, H&E liver nodule), 125 µm (D, H&E nodules), 5 mm (E, NIR2), and 2.5 mm (E, SPARC, AF750–M13).]

specificity of the probe toward tumor nodules compared with its underlying organs.

The in vivo sensitivity of targeting conferred by the SBP was assessed by injecting tumor-bearing animals with M13–SWNTs expressing SBPs or untargeted M13–SWNTs. The NIR2 intensities of excised tumor nodules and intestinal tissue of the same animal were used to compute TBRs for the targeted and untargeted probes. SBP–M13–SWNTs showed significant, 10-fold higher TBRs than untargeted M13–SWNTs, likely due to a combination of improved targeting and reduced tissue autofluorescence in the NIR2 window (Fig. 3C).

To verify the specificity of SBP–M13–SWNTs, we assessed the SWNT-positive tumor nodules by immunohistochemistry. Standard hematoxylin and eosin (H&E) staining of SWNT-positive tumor sections revealed histopathological features consistent with ovarian tumor nodules, including a high nuclear-to-cytoplasmic ratio, cellular crowding, a necrotic core, and a distinct architecture from underlying organs (Fig. 3D). Interestingly, the liver exhibits a fluorescent signal where no tumor nodule is visible by the eye, and after biopsy of the indicated area, H&E staining indicated pathology consistent with tumor nodules located on the liver (Fig. 3D, Upper). Additionally, immunohistochemical staining revealed an enrichment of SPARC expression along the periphery of the SWNT-positive tumor nodules (SI Appendix, Fig. S8). Finally, to assess whether our probe specifically colocalizes with SPARC-expressing regions of the tumor nodules, we administered SBP–M13–SWNTs conjugated with AlexaFluor750 to tumor-bearing mice and analyzed the excised tumor nodules by immunofluorescence. In multiple nodules, SPARC was widely expressed, with particularly strong expression at the tumor periphery (Fig. 3E, Middle) in a pattern consistent with our immunohistochemical staining described in SI Appendix, Fig. S8. The AF750-labeled SBP–M13–SWNTs were similarly enriched at the tumor periphery (Fig. 3E, Bottom). These patterns are consistent with an outside–in diffusion model limited both by the hydrodynamic radius and ligand interactions of SBP–M13–SWNTs with the tumor nodule.

Image Guidance Using SBP–M13–SWNT Improves Surgical Resection of Tumors. To assess the potential clinical utility of SBP–M13–SWNTs for reduction of tumor burden, a gynecological surgeon performed surgeries on orthotopic models of ovarian cancer that were imaged at various points during the surgical procedures. Approximately 15–25 min were spent on procedures in each experiment, and tumor implants were predominantly distributed in the bowel mesentery, peritoneal wall, subdiaphragmatic surfaces, and surfaces of organs including the liver, spleen, pancreas, and within the pelvic cavity. H&E-stained tissue sections were prepared from all excised nodules and assessed by a pathologist. With the exception of two non–tumor-containing mesenteric lymph nodes, all tissues examined (n = 197) were positive for ovarian tumor tissue, indicating an accuracy of 98.9% of our probe for ovarian tumors. Surgery was first performed with preoperative image guidance to assess whether this addition to the process would be beneficial to the surgical procedure based on the distribution of excised tumor nodule sizes. A comparative analysis of excised tumors revealed that a significantly higher number of submillimeter tumor nodules were discovered in the image-guided cohorts versus the non–image-guided cohorts (12 and 0 nodules, respectively; SI Appendix, Fig. S11). Using image guidance, there were also greater numbers of excised tumors from 1.3 to 3 mm; however, there was no appreciable difference for larger tumors (>3 mm) between image-guided and non–image-guided cohorts. We additionally assessed the impact of performing surgery in a serial manner, with an initial round of non–image-guided surgery, followed by image acquisition and a second round of image-guided surgery (Fig. 4A). We observed reduction of tumor burden from non–image-guided surgery to image-guided surgery
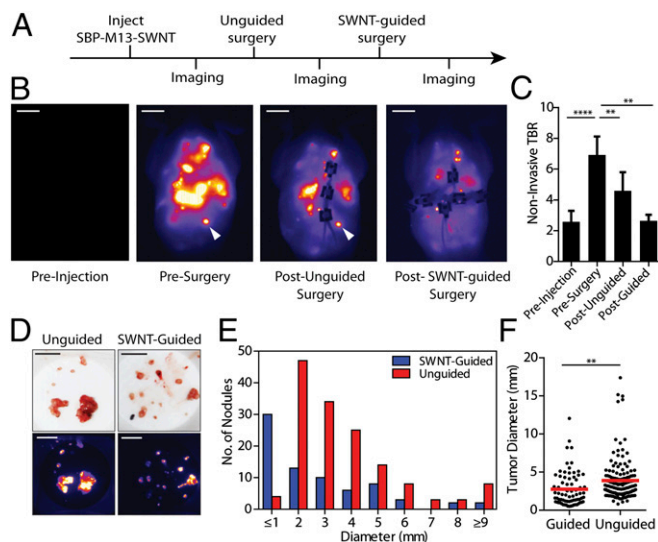
MEDICAL SCIENCES

ENGINEERING

Fig. 4. Surgical removal of tumors with SBP–M13–SWNT guidance. (*A*) Schematic of serial surgical procedure. (*B*) Representative whole-abdomen NIR2 images before injection of SBP–M13–SWNT, before surgery, after an initial unguided surgery, and after subsequent SBP–M13–SWNT-guided surgery. White arrow indicates an SWNT-positive nodule detected only during image-guided surgery. (*C*) TBRs during surgery. Muscle from the hind limb was used for background (**$P < 0.01$; ****$P < 0.0001$; two-tailed t tests; error bars represent SE). (*D*) Photographs and NIR2 images of excised tumor nodules following unguided and SWNT-guided surgery. (*E*) Histogram of tumor diameters removed with and without guidance. (*F*) Dot plot of individual tumor nodule diameters excised with and without SWNT-guidance (guided, $n = 74$; unguided, $n = 146$; **$P < 0.01$; two-tailed t test). [Scale bars, 1 cm (*B*), 1 cm (*C*, photograph), and 1 cm (*C*, NIR2).]

(Fig. 4*B*). We determined the TBR of overall tumor burden to background muscle by region of interest analysis and confirmed reduction of overall tumor burden due to image-guided reduction (Fig. 4*C*). Using both SWNT imaging (Fig. 4*B*) and quantification of excised tumor nodule diameters, we observed a greater number of submillimeter excised tumors in the groups assisted by SWNT image guidance (30 versus 4 nodules; Fig. 4 *D* and *E*). Overall, significantly more, smaller diameter tumors were excised using SWNT-based image guidance as opposed to unguided surgeries (Fig. 4*F*).

Discussion

This study describes the development and use of a single fluorescence imaging agent for high-contrast, detection and guidance for surgical removal of disseminated ovarian tumors. NIR2-emitting SWNT probes offer significantly improved signal-to-noise performance compared with visible and near-infrared dyes and detect tumors not visualized using the optical dyes. These targeted, M13-stabilized SWNT probes assist surgical removal of ovarian tumors with excellent sensitivity, as confirmed by subsequent pathological examination. The probe is sensitive for identifying tumor nodules located on several abdominal viscera, the peritoneal wall, and the bowel mesentery. Importantly, compared with fluorescent probes in the visible or NIR1 regimes, the fluorescence of SWNTs is not limited by quenching, allowing for long-term, continuous imaging. With the development of advanced imaging platforms, surgeons may be able to visualize tumors both before and throughout surgical procedures, thereby significantly improving fluorescence-guided tumor resection. This study demonstrates that surgery accompanied by image guidance leads to identification and removal of smaller tumor nodules. Although NIR2 images could not provide 3D localization of the tumor implants, they provided information about the

sites of disease burden requiring closer surgical examination. Imaging of regions in which the surgeon was initially reluctant to explore in an effort to minimize morbidity by risking excessive blood loss, but were shown to harbor a positive NIR2 signal, often led to the identification and excision of additional tumor nodules missed on non–image-guided approaches. Although we did not investigate longitudinal survival rates after image-guided surgery due to surgical constraints in our small-animal models, the majority of clinical evidence suggests that optimal surgery, currently defined as the removal of tumors with diameters of 1 cm and larger, is correlated with improved overall survival rates (16). SWNT-based affinity probes may aid in surgical planning and resection to help achieve a reduction in mortality rates in the future.

We achieve detection of submillimeter tumors with excellent TBRs using M13-stabilized SWNTs, in part due to properties of the particles that lead to low tissue scattering and minimal tissue autofluorescence in the NIR2 optical window. In comparing excised tumors with unaffected intestinal tissues as a background measurement, we observed high TBRs of ~112 using our SPARC-targeted M13–SWNT probes. Following i.p. administration, some uptake is observed using nontargeted SWNT probes, which is most likely due to nonspecific binding interactions or convective flow patterns present within the peritoneal cavity. Whereas many nanoparticles include targeting peptides conjugated directly to the nanoparticle, our nanoprobe takes advantage of the genetically encoded M13 scaffold to spatially uncouple the targeting peptide (SBP) from the imaging probe (SWNT). This separation of targeting and imaging moieties circumvents direct and excessive conjugation, which may abolish the functionality of each component (11, 26); however, how this spatial uncoupling affects both targeting and nanomaterial functionality is an area requiring further study.

Fluorescence imaging in the second optical window offers the promise of imaging at greater penetration depths (>3–5 mm) with reduced optical scattering within the tissue. In comparing the performance of visible, NIR1, and NIR2 probes, the M13–SWNT probe achieved the highest tumor-to-muscle ratios and TBRs, most likely due to less tissue absorbance and autofluorescence in the NIR2 regime. In addition, we were able to see tumors not observed in the visible and NIR channels, highlighting the improved tissue penetration and detection in the NIR2 regime. Using our reflectance imaging system, we can detect 1-mm-diameter tumors up to a maximal depth between 9.7 and 18.2 mm. To our knowledge, this represents the highest reported depth of detection using fluorescence reflectance and is also higher than previous reports that detected mammary tumors labeled with activatable Cy5 probes (3). Future work to enhance the fluorescence of M13–SWNTs using plasmonic nanomaterials (27) and affinity targeting using other ligand–receptor interactions including the folate receptor (4) may offer further improvements on current limits of detection and resolution. These longer wavelength-emitting probes will greatly aid in locating ovarian tumors confined to deep anatomical regions.

SBP–M13–SWNTs injected intraperitoneally colocalized with stromal SPARC expression on the periphery of the ovarian tumor nodules. Tumor nodules labeled with the probes exhibited high signal with low background in the surrounding healthy tissues, including liver, spleen, and intestine. These high organ-specific TBRs contributed to more accurate surgical resection of tumor nodules localized to the organ surfaces. Because our probes can visualize the tumor margins, they have potential to assist the surgeon in delineating tumors from healthy tissue for improved resection of other solid tumors, as also demonstrated by approaches using activatable peptides (3, 28) and dyes (2), fluorescein conjugates (4), and multimodal nanoparticles (29).

The use of nanomaterials as clinical imaging probes is a rapidly evolving area. As new materials emerge from the community, their attractiveness for clinical applications is typically

informed first by their in vitro properties, then by their behavior in animal models, and ultimately by their performance in humans. In this context, M13–SWNT probes exhibit many desirable in vitro properties such as solution stability, retention of optical properties under various pH and physiological environments and under constant excitation, and the dual capability of genetically encoding affinity ligands and solubilizing SWNTs. The next step in assessing their attractiveness for clinical translation is to assess their performance in animal models. Thus, this study explores the roles of targeting, acute biocompatibility via i.p. delivery, and optical emission in NIR2 in a preclinical mouse model of ovarian cancer. Our acute toxicity studies are consistent with several other preliminary studies exploring the safety of M13 and SWNTs, in that a panel of serum biomarkers were not elevated (30–33). Collectively, we believe these findings suggest that these materials warrant further consideration for clinical translation, which would include the development of instruments for real-time imaging, outcomes research such as survival studies in preclinical models, and rigorous safety evaluation through the National Characterization Laboratory (National Cancer Institute) and others to assess long-term trafficking and clearance of these materials as well as chronic toxicity studies.

Although in this study we use SWNTs for fluorescence imaging, others have demonstrated their utility as carriers for therapeutic cargoes (reviewed in ref. 34) as well as photothermal ablative therapy (35). We have begun to explore the utility of SBP–M13–SWNTs for in vivo heating of the tumor microenvironment to assess their potential as sensitizing agents to multimodal imaging and therapeutic agents.

To advance our findings closer to clinical translation, new instrumentation will be required to allow for real-time intraoperative guidance and 3D tomography for quantitative analysis and more accurate localization of tumors. Simulations suggest that at near-infrared wavelengths that define the NIR2 window, SWNT-based probes may be detectable at depths up to 10 cm on improved imaging platforms, highlighting the potential utility of these particles in human subjects (36). This new platform would allow for real-time, noninvasive imaging and processing for visualization of tumors during tumor staging, presurgical planning, and procedures. Coupling improved instrumentation with probe development will greatly improve the ability to detect tumors at earlier stages. The instrumentation should also be compatible with other NIR2 window optical probes as they are developed. Early detection of smaller tumors may also provide fundamental insights into tumorigenesis and disease progression, as well as allow clinicians to better monitor therapeutic responses and recurrence of disease.

Materials and Methods

All materials are provided in *SI Appendix, SI Materials and Methods*. In vitro and in vivo characterization of the SBP–M13–SWNT probe, including optical properties, stability, detection sensitivity, biodistribution, and serum chemistry assays, are described in detail in *SI Appendix, SI Materials and Methods*. Tumor induction procedure, fluorescence imaging, and analysis of SBP–M13–SWNT targeting in vivo and ex vivo are detailed in *SI Appendix, SI Materials and Methods*. Comparison of noninvasive imaging between SBP–M13–SWNT with visible and NIR1 imaging probes and image-guided surgeries is described in *SI Appendix, SI Materials and Methods*.

1. Weissleder R, Pittet MJ (2008) Imaging in the era of molecular oncology. *Nature* 452(7187):580–589.
2. Urano Y, et al. (2011) Rapid cancer detection by topically spraying a γ-glutamyl-transpeptidase-activated fluorescent probe. *Sci Transl Med* 3(110):ra119.
3. Nguyen QT, et al. (2010) Surgery with molecular fluorescence imaging using activatable cell-penetrating peptides decreases residual cancer and improves survival. *Proc Natl Acad Sci USA* 107(9):4317–4322.
4. van Dam GM, et al. (2011) Intraoperative tumor-specific fluorescence imaging in ovarian cancer by folate receptor-α targeting: First in-human results. *Nat Med* 17(10):1315–1319.
5. Lim YT, et al. (2003) Selection of quantum dot wavelengths for biomedical assays and imaging. *Mol Imaging* 2(1):50–64.
6. Troy TL, Thennadil SN (2001) Optical properties of human skin in the near infrared wavelength range of 1000 to 2200 nm. *J Biomed Opt* 6(2):167–176.
7. Heller DA, et al. (2004) Concomitant length and diameter separation of single-walled carbon nanotubes. *J Am Chem Soc* 126(44):14567–14573.
8. Yi H, et al. (2012) M13 phage-functionalized single-walled carbon nanotubes as nanoprobes for second near-infrared window fluorescence imaging of targeted tumors. *Nano Lett* 12(3):1176–1183.
9. Welsher K, Sherlock SP, Dai H (2011) Deep-tissue anatomical imaging of mice using carbon nanotube fluorophores in the second near-infrared window. *Proc Natl Acad Sci USA* 108(22):8943–8948.
10. Ghosh D, et al. (2012) M13-templated magnetic nanoparticles for targeted in vivo imaging of prostate cancer. *Nat Nanotechnol* 7(10):677–682.
11. Gu F, et al. (2008) Precise engineering of targeted nanoparticles by using self-assembled biointegrated block copolymers. *Proc Natl Acad Sci USA* 105(7):2586–2591.
12. Poon Z, et al. (2010) Ligand-clustered "patchy" nanoparticles for modulated cellular uptake and in vivo tumor targeting. *Angew Chem Int Ed Engl* 49(40):7266–7270.
13. Akerman ME, Chan WCW, Laakkonen P, Bhatia SN, Ruoslahti E (2002) Nanocrystal targeting in vivo. *Proc Natl Acad Sci USA* 99(20):12617–12621.
14. Ruoslahti E, Bhatia SN, Sailor MJ (2010) Targeting of drugs and nanoparticles to tumors. *J Cell Biol* 188(6):759–768.
15. Jemal A, et al. (2011) Global cancer statistics. *CA Cancer J Clin* 61(2):69–90.
16. Chi DS, et al. (2006) What is the optimal goal of primary cytoreductive surgery for bulky stage IIIC epithelial ovarian carcinoma (EOC)? *Gynecol Oncol* 103(2):559–564.
17. Scott JK, Smith GP (1990) Searching for peptide ligands with an epitope library. *Science* 249(4967):386–390.
18. Pasqualini R, Ruoslahti E (1996) Organ targeting in vivo using phage display peptide libraries. *Nature* 380(6572):364–366.
19. Lee YJ, et al. (2009) Fabricating genetically engineered high-power lithium-ion batteries using multiple virus genes. *Science* 324(5930):1051–1055.
20. Dang X, et al. (2011) Virus-templated self-assembled single-walled carbon nanotubes for highly efficient electron collection in photovoltaic devices. *Nat Nanotechnol* 6(6):377–384.
21. Kelly KA, Waterman P, Weissleder R (2006) In vivo imaging of molecularly targeted phage. *Neoplasia* 8(12):1011–1018.
22. Chen J, et al. (2012) SPARC is a key regulator of proliferation, apoptosis and invasion in human ovarian cancer. *PLoS ONE* 7(8):e42413.
23. Cherukuri P, et al. (2006) Mammalian pharmacokinetics of carbon nanotubes using intrinsic near-infrared fluorescence. *Proc Natl Acad Sci USA* 103(50):18882–18886.
24. Derfus AM, Chan WCW, Bhatia SN (2004) Probing the cytotoxicity of semiconductor quantum dots. *Nano Lett* 4(1):11–18.
25. Rhodes DR, et al. (2004) ONCOMINE: A cancer microarray database and integrated data-mining platform. *Neoplasia* 6(1):1–6.
26. Hlavacek WS, Posner RG, Perelson AS (1999) Steric effects on multivalent ligand-receptor binding: Exclusion of ligand sites by bound cell surface receptors. *Biophys J* 76(6):3031–3043.
27. Hong G, et al. (2010) Metal-enhanced fluorescence of carbon nanotubes. *J Am Chem Soc* 132(45):15920–15923.
28. Olson ES, et al. (2010) Activatable cell penetrating peptides linked to nanoparticles as dual probes for in vivo fluorescence and MR imaging of proteases. *Proc Natl Acad Sci USA* 107(9):4311–4316.
29. Kircher MF, et al. (2012) A brain tumor molecular imaging strategy using a new triple-modality MRI-photoacoustic-Raman nanoparticle. *Nat Med* 18(5):829–834.
30. Krag DN, et al. (2006) Selection of tumor-binding ligands in cancer patients with phage display libraries. *Cancer Res* 66(15):7724–7733.
31. Kolosnjaj-Tabi J, et al. (2010) In vivo behavior of large doses of ultrashort and full-length single-walled carbon nanotubes after oral and intraperitoneal administration to Swiss mice. *ACS Nano* 4(3):1481–1492.
32. Liu Z, et al. (2008) Circulation and long-term fate of functionalized, biocompatible single-walled carbon nanotubes in mice probed by Raman spectroscopy. *Proc Natl Acad Sci USA* 105(5):1410–1415.
33. Schipper ML, et al. (2008) A pilot toxicology study of single-walled carbon nanotubes in a small sample of mice. *Nat Nanotechnol* 3(4):216–221.
34. Liu Z, Tabakman S, Welsher K, Dai H (2009) Carbon nanotubes in biology and medicine: In vitro and in vivo detection, imaging and drug delivery. *Nano Res* 2(2):85–120.
35. Kam NW, O'Connell M, Wisdom JA, Dai H (2005) Carbon nanotubes as multifunctional biological transporters and near-infrared agents for selective cancer cell destruction. *Proc Natl Acad Sci USA* 102(33):11600–11605.
36. Kim S, et al. (2004) Near-infrared fluorescent type II quantum dots for sentinel lymph node mapping. *Nat Biotechnol* 22(1):93–97.

MEDICAL SCIENCES

ENGINEERING

Supplementary Information

Title: Deep, noninvasive imaging and surgical guidance of submillimeter tumors using targeted M13-stabilized single-walled carbon nanotubes

Short title: Tumor imaging and surgery using carbon nanotubes

Authors: Debadyuti Ghosh[a,b,1,2], Alexander F. Bagley[a,c,d,1], Young Jeong Na[e], Michael Birrer[e], Sangeeta N. Bhatia[a,f,g,h,i,3,4], Angela M. Belcher[a,b,j,3,4]

Affiliations:

[a]Koch Institute for Integrative Cancer Research, Massachusetts Institute of Technology, Cambridge, Massachusetts, 02139.

[b]Department of Materials Science and Engineering, Massachusetts Institute of Technology, Cambridge, Massachusetts, 02139.

[c]Biophysics Program, Harvard University, Boston, Massachusetts, 02115.

[d]MD-PhD Program, Harvard Medical School, Boston, Massachusetts, 02115.

[e]Department of Medicine, Massachusetts General Hospital, Harvard Medical School, Boston, Massachusetts, 02114.

[f]Harvard-MIT Division of Health Sciences and Technology, Cambridge, Massachusetts, 02139.

[g]Department of Electrical Engineering and Computer Science, Massachusetts Institute of Technology, Cambridge, Massachusetts, 02139.

[h]Institute for Medical Engineering and Science, Cambridge, Massachusetts, 02139.

[i]Howard Hughes Medical Institute, Massachusetts Institute of Technology, Cambridge, Massachusetts, 02139.

[j]Department of Biological Engineering, Massachusetts Institute of Technology, Cambridge, Massachusetts, 02139.

[1]D.G. and A.F.B. contributed equally to this work.

[2]Present address: Division of Pharmaceutics, College of Pharmacy, The University of Texas at

Austin, Austin, Texas, 78712.

[3]S.N.B. and A.M.B. contributed equally to this work.

[4]To whom correspondence may be addressed:

Sangeeta N. Bhatia, 77 Massachusetts Ave., 76-453, Cambridge, Massachusetts, 02139,

Phone: 617-253-0893, email: sbhatia@mit.edu

Angela M. Belcher, 77 Massachusetts Ave., 76-561, Cambridge, Massachusetts, 02139, Phone:

617-324-2800, email: belcher@mit.edu

SI Materials and Methods

Genetic engineering of SPARC binding peptide (SBP) onto p3 of SWNT-binding M13 phage

Genetic engineering of the SPARC binding peptide (designated as SBP) and SWNT-binding peptide (designated as DSPH) was described previously (1). Briefly, oligonucleotides encoding SPARC binding peptide (designated as SBP, SPPTGINGGG (1-3)), 5'(Phos)-GTA CCT TTC TAT TCT CAC TCT TCA CCA CCG ACT GGA ATT AAC GGA GGC GGG TC -3' and 5'(Phos)-GGC CGA CCC GCC TCC GTT AAT TCC AGT CGG TGG TGA AGA GTG AGA ATA GAA AG-3' (IDT) were annealed and inserted into the EagI and Acc65I restriction endonuclease sites of double stranded M13 DNA for N-terminal display on p3. The M13-based cloning vector was isolated from the SWNT-binding phage using standard DNA isolation (QIAGEN). Ligations were transformed in electrocompetent XL-1 Blue cells (Agilent Technologies), plated in top agar and incubated at 37°C overnight. DNA was purified (Qiagen) from isolated blue plaques and sequenced to confirm the insertion of SBP on p3.

SBP-M13-SWNT Complexation

To prepare the starting SWNTs (1, 4), non-acid treated HiPCO SWNTs (Unidym) were diluted in aqueous 2 wt% sodium cholate (SC). The solution was then homogenized for 1 h, cup-horn sonicated for 10 min at 90% amplitude and then centrifuged at 30,000 rpm for 4 h to disperse individual SWNTs. SWNT concentration was determined by measuring absorbance at 632 nm and calculated using the extinction coefficient of HiPCO SWNT at 632 nm, $\varepsilon_{632\,nm}$=0.036 L/mg•cm. Complexation of M13 to SWNT was performed as previously described (1). Briefly, the calculated amount of SWNT-binding phage solution was mixed with the calculated volume of SWNTs dispersed by 2 wt% SC in water to achieve a 1:1 stoichiometric ratio of phage-to-SWNT. The solution was placed in a dialysis membrane with MWCO 12,000-14,000 and dialyzed against water (10 mM NaCl, pH =5.3) for 48 hours with frequent buffer exchange. pH of

the dialyzing solution was increased to 10 after 48 hours of dialysis. After dialysis, the phage-SWNT complex was removed and placed in a conical tube. Prior to experiments, samples were resuspended in 1x PBS, vortexed and centrifuged at 6000 rpm for 5 min. To assess reproducibility of SBP-M13-SWNT complexation, three separate batches of 1E14 SBP-M13-DSPH virus resuspended in double distilled water were mixed at a 1:1 stoichiometric ratio with HiPCO SWNTs initially dispersed in 2% wt SC. Complexing was performed as described above. To confirm reproducibility of batches, the absorbance of the samples was measured by uv-vis spectrophotometry. The spectra of each batch were read three times.

Absorbance and PLE measurements

Absorption measurements were taken with a DU800 spectrophotometer (Beckman Coulter). PL of SWNT was measured with a FluoroMax spectrofluorometer (Horiba Jobin Yvon).

Imager Setup

For fluorescence imaging in the second optical window, an in-house *in vivo* imager was previously described (1). A liquid nitrogen-cooled OMA V 2D InGaAs array detector (detection range: 800 – 1,700 nm) with a 256 × 320 pixel array (Princeton Instruments) was used with a NIR camera lens (SWIR-25, Navitar) attached in front of the detector. To reduce tissue autofluorescence and maximize the detection of fluorescence from SWNTs, two stacked long-pass filters with cut-off wavelength of 1,100 nm and OD >4 (EdmundOptics) were used. For excitation, an optical fiber coupled to an 808 nm diode laser (MDL-F-808, OptoEngines) was used and a laser line filter with center wavelength of 808 nm (Edmund Optics) was attached in front of the laser to remove unwanted excitation light. To minimize laser exposure to animals, a computer-controlled shutter was incorporated into the imaging system. The measured fluence on the mouse for *in vivo* imaging was ~100 mW/cm^2. The acquisition time for *in vivo* imaging

ranged from 0.01 s – 1 s. For white contrast images, the same detector was used but the mice were illuminated with white light.

Blood and Ascites Stability and pH Measurements

For blood stability measurements, 20 ug/mL SBP-M13-SWNT was diluted in two-fold dilutions with PBS and then diluted 1:1 volume with blood obtained from healthy mice (Research Blood Components) and incubated for 0, 1, 2, 4, and 24 h. Samples were measured at the given time point using the NIR2 imager at 0.01 s exposure. For pH stability, SBP-M13-SWNT were calibrated to pH = 4.5, 5.5. 6.5, 7.5, or 8.5 and samples were incubated 0, 1, 2, 4, and 24 h. Samples were measured using NIR2 imager at 0.01 s exposure.

Photobleaching of SBP-M13-SWNT

SBP-M13-SWNTs were exposed under constant irradiation for 30 minutes using an 808 nm laser from the NIR2 imager setup. At every 5 minutes, samples would be measured using the NIR2 imager from exposures ranging from 0.01 to 1 s. Error bars denote s.d.

Cell Viability Assay

To confirm HUVEC and OVCAR8 viability in the presence of SBP-M13-SWNT, 5,000 cells were seeded on 96 well plate and incubated with 10, 5, 2.5, 1.25, 0.62, and 0 ug/mL SBP-M13-SWNT. Twenty-four hours after probe incubation, Alamar Blue (Life Technologies) was added and fluorescence was measured 4 h post-addition, following manufacturer's recommendations. Viability was normalized to blank control. Samples were run in quadruplicate.

Sensitivity of Probe in Cell Culture

Serial tenfold dilutions of OVCAR8 cells were plated in 24 well plates and incubated with ~20-30 ug/mL SBP-M13-SWNT. After 24 hours incubation, cells were washed and lysed.

Samples were measured using NIR2 imager at 0.01 s exposure. Samples were run in triplicate and error was denoted as standard error.

Cell Culture and Establishment of an Orthotopic Ovarian Cancer Model

All animal studies and procedures were approved by the MIT Institutional Animal Care and Use Committee. This study used the established human ovarian epithelial carcinoma cell line OVCAR8, engineered to constitutively express firefly luciferase. OVCAR8 cells were grown in RPMI 1640 medium containing 10% fetal bovine serum, penicillin, and streptomycin. Approximately 2 x 10^6 OVCAR8 cells suspended in 200 μL phenol-red free DMEM (Invitrogen) were implanted into the peritoneal cavity of athymic (*nu/nu*) mice to establish orthotopic ovarian cancer models. Mice were monitored by whole-animal bioluminescence imaging to assess tumor burden. Imaging experiments were performed approximately 7-14 days following tumor cell injection based on the measured bioluminescent intensity.

Intravenous versus intraperitoneal administration of SBP-M13-SWNT

To compare routes of administration, SBP-M13-SWNT was injected i.v. or i.p. in tumor-bearing mice. Blood was collected from tail-vein at 0, 10, 30, 60 and 150 minutes post-injection. Blood was measured for fluorescence from circulating SWNT probe using NIR2 imager at 0.1 s exposure.

Comparison of Non-Invasive Imaging *In Vivo* Between SBP-M13-SWNT, Near-Infrared and Visible Dyes

To confirm improved signal-to-noise in the NIR2 regime, SBP-M13-SWNT was compared with SBP-M13 conjugated to a NIR dye, Alexa Fluor 750 (designated as SBP-M13-AF750), and a visible dye, fluorescein isothiocyanate (SBP-M13-FITC). To determine the detection limit of the probes, two-fold dilutions of SBP-M13-SWNT, SBP-M13-750 and SBP-

M13-FITC were prepared onto a microtiter plate and their fluorescence was measured using either the custom-built NIR2 reflectance imager or an IVIS Spectrum, respectively. Samples were measured within the linear range of detection, set from 1000 to 60000 for each instrument. Images were acquired under various exposure times, from 0.01 s to 10 s. Fluorescence from SBP-M13-SWNT was measured using the custom-built NIR2 reflectance imager at maximum aperture, with a laser power of ~100 mW/cm^2 at 0.01, 0.05, 0.1, 0.5, and 1 s exposures. SBP-M13-750 or SBP-M13-FITC was measured using an IVIS Spectrum in epi-illumination mode, under highest power, with fstop1 or fstop2 aperture (maximum and second-highest aperture) at 0.5, 1, 2, 5, and 10 s exposures. Regions of interest (ROIs) were drawn around microtiter wells and fluorescence counts were determined for samples in the linear range (i.e. 1000 – 60000) using ImageJ software. The limit of detection of the probe was determined to be the minimum concentration detectable by the imaging system within the linear range.

To compare signal-to-noise *in vivo* between the fluorescence probes, probes were combined and added in five-fold excess of their detection limit to mice bearing disseminated OVCAR8 tumors. Fluorescence images from SBP-M13-SWNT and SBP-M13-750/SBP-M13-FITC were acquired using the NIR2 imager and IVIS, respectively. Images obtained from NIR2 imager were taken at 0.01, 0.05, 0.1, 0.5, and 1 s exposures. Images taken using the IVIS Spectrum were acquired at 0.5, 1, 2, 5, and 10 s exposures. All images were analyzed using ImageJ software. ROIs were drawn over the peritoneal cavity containing tumors, muscle, and background of the images. Fluorescence intensities were determined from the ROIs and tumor-to-muscle and tumor-to-background ratios were calculated. Samples were run with standard error (n = 3).

Depth of Detection Limit of Tumors Labeled with SBP-M13-SWNT

Mice bearing OVCAR8 tumors were injected with ~200 ug/kg SBP-M13-SWNT. Twenty-four hours post-injection, tumors were excised. To determine the limit of detection by reflectance

imaging, labeled tumors were cut into 1 mm diameter fragments and placed in a quartz capillary tube (Sutter Instruments). The quartz capillary tube was placed in a XFM-2 phantom mouse (Caliper) with the same optical properties of human tissue at 0, 4.3, 7.0, 9.7, or 18.2 mm depths. The fluorescence from the labeled tumor fragments was measured using the NIR2 imager at maximum aperture using 0.5 s exposure time. Background fluorescence images were also acquired before addition of labeled tumors. To quantify detection depth, background images were subtracted from acquired images of fluorescent tumors, and equivalent ROIs were drawn for images taken from each depth to calculated signal intensity.

In vivo Fluorescence Imaging of SBP-M13-SWNTs

SBP-M13-SWNTs were injected into the peritoneal cavity of tumor-bearing animals at ≈200 μg/kg. Mice were anesthetized with isoflurane gas. Fluorescence images were obtained approximately 24 hours following injection with exposure times ranging from 0.01 to 1 second for each subject. Background images were subtracted from raw images to generate the final images. We constructed equivalent standardized regions of interest (ROIs) to determine tumor-to-background ratios at various locations within the peritoneal cavity. For comparisons of SBP-targeted and untargeted M13-SWNT probes, we compared NIR fluorescent intensities of excised tumor nodules with normal intestinal tissue. Image intensities were quantified with ImageJ software.

SBP-M13-SWNT Imaging During Surgery

Surgical studies were performed by a gynecologic surgeon. Animals were administered ≈200 μg/kg SBP-M13-SWNTs approximately 24 hours prior to surgery. For comparisons of initial surgery with or without SWNT-guidance, animals were randomly assigned to one of these cohorts, and NIR2 fluorescence images were obtained 2-4 hours prior to surgery for all animals. For animals assigned to the SWNT-guided cohort, the whole-abdomen NIR2 fluorescence

images were assessed by the surgeon prior to and during the surgical procedure. Excised nodules were measured, photographed, and imaged for SWNT-based fluorescence.

Immunohistochemistry and fluorescence

Excised tissues were fixed in 10% formalin, embedded in paraffin, and sectioned for histology. Hematoxylin and eosin (H&E) staining was performed on tissue sections. For SPARC staining, rat anti-SPARC (1:40 dilution, R&D Systems) and rat isotype IgG (1:200, Abcam) were used with biotin-conjugated goat anti-rat antibody (Vector Labs, BA-9401), followed by the Vectastain ABC immunoperoxidase kit (Vector Labs, PA-6100) and DAB substrate (Vector Labs, SK-4100) for detection and visualization. For immunofluorescence, Alexa Fluor donkey anti-rat 488 secondary antibodies (Life Technologies) were used on frozen tissue sections. To visualize SBP-M13-SWNT by fluorescence, Alexa fluor 750 carboxylic acid, succinimidyl ester (Life Technologies) was conjugated to SBP-M13-SWNT via primary amine linkage following manufacturer's recommendations and excess dye was removed by extensive dialysis before usage.

Serum chemistry and biodistribution studies

Animals bearing orthotopic OVCAR8 xenograft tumors were administered SBP-M13-SWNTs labeled with AF750 dye or control PBS into the peritoneal cavity. After 24 hours or one week following probe administration, blood was collected from animals via intracardiac puncture and immediately transferred to serum-separator collection tubes (BD Vacutainer SST). Samples were incubated at room temperature for 30 minutes, centrifuged at 1,000 x g for 10 minutes, and placed on ice. Serum samples were transferred to the MIT Comparative Pathology Laboratory for metabolic and enzymatic profiling. For biodistribution studies, organs were harvested at the given time points from euthanized animals, rinsed briefly in PBS, and fluorescence of whole organs was measured using an NIR imaging system (LICOR Odyssey).

For skin and peritoneal membrane, tissue samples were obtained in proximity to the injection site. Mean fluorescence intensity of each tissue was quantified using ImageJ software and all statistical analysis was performed using GraphPad Prism software.
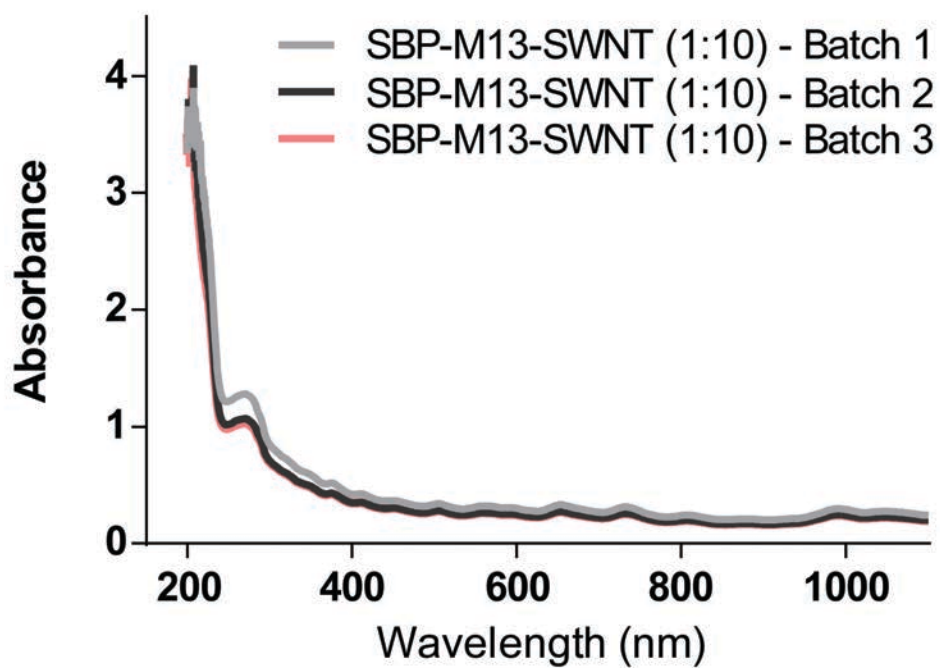
Figure S1.

Fig. S1. Absorbance spectra for SBP-M13-SWNT batches. Each batch was measured in triplicate at a 1:10 dilution in water and spectra represent mean absorbance within each batch.
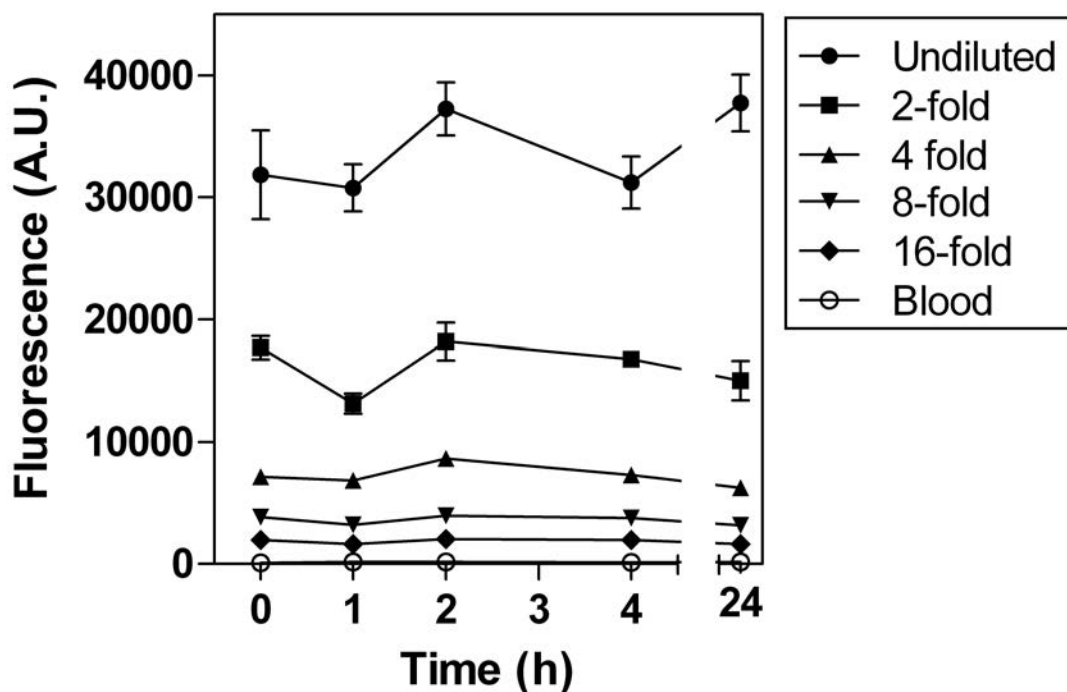
Figure S2.

Fig. S2. Stability of SBP-M13-SWNTs in blood. Serial two-fold dilutions of SBP-M13-SWNTs were incubated in blood to assess detection range and stability of the imaging probe in an *in vivo* environment for periods up to 24 hours. NIR2 fluorescence measurements directly correlated with concentration of SBP-M13-SWNT, and the fluorescence remained stable for periods up to 24 hours. Dilutions were measured in duplicate. Error bars denote standard deviation.
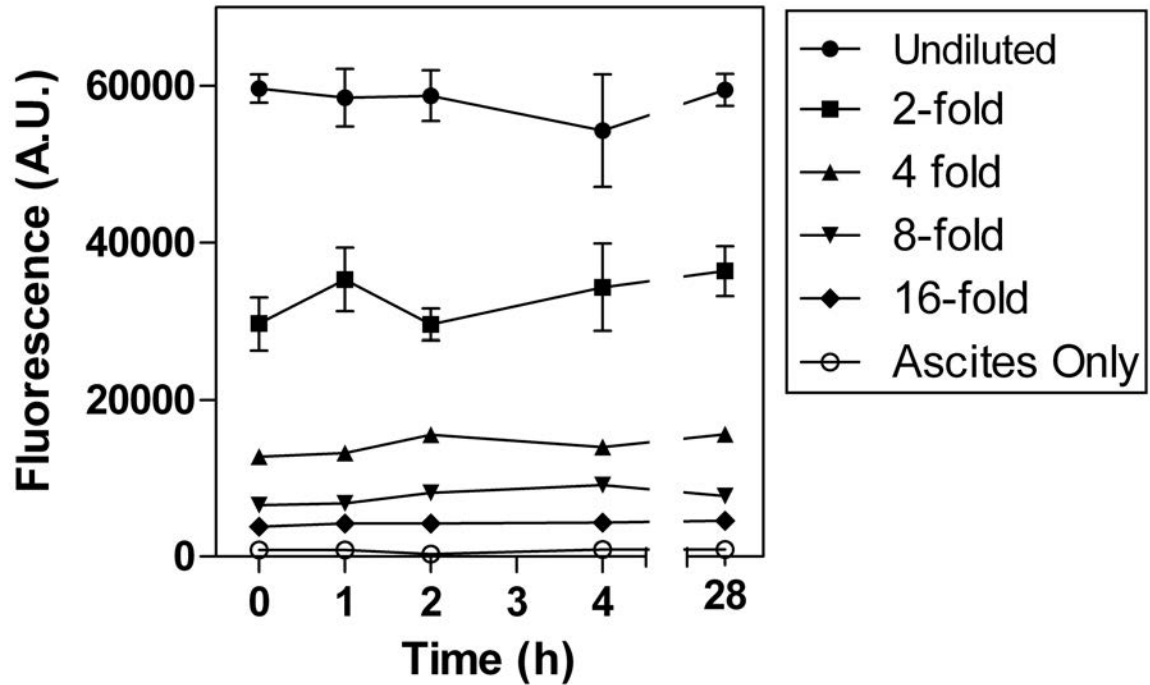
Fig. S3. Stability of SBP-M13-SWNTs in ascites. Serial two-fold dilutions of SBP-M13-SWNTs were incubated in ascites harvested from a tumor-bearing mouse to assess stability and detection limit of the imaging probe for periods up to 28 hours. Fluorescent signal was directly proportional to concentration of SBP-M13-SWNT in ascites. Dilutions were measured in duplicate. Error bars denote standard deviation.

Figure S4.
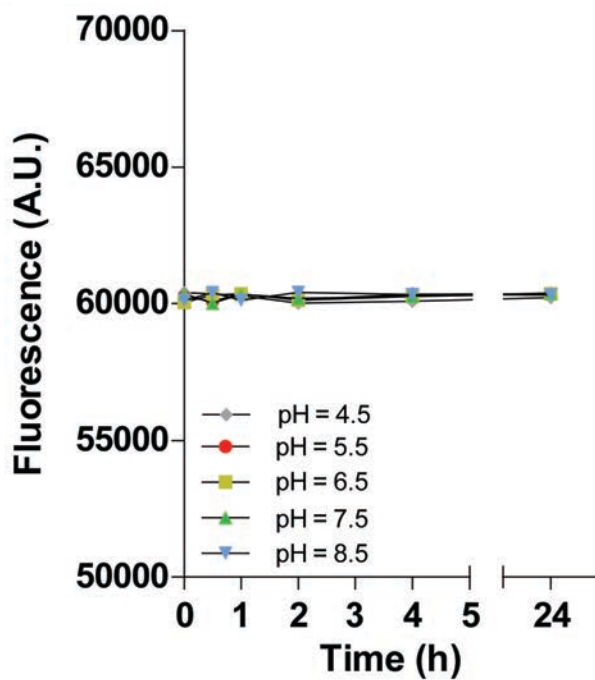
Fig. S4. pH stability of SBP-M13-SWNTs. SBP-M13-SWNTs were incubated at pHs between 4.5 – 8.5 for periods up to 24 hours. NIR2 fluorescence measurements were unaffected by pH of the solution for periods up to 24 hours. Samples were measured in duplicate. Error bars denote standard error.

Figure S5.
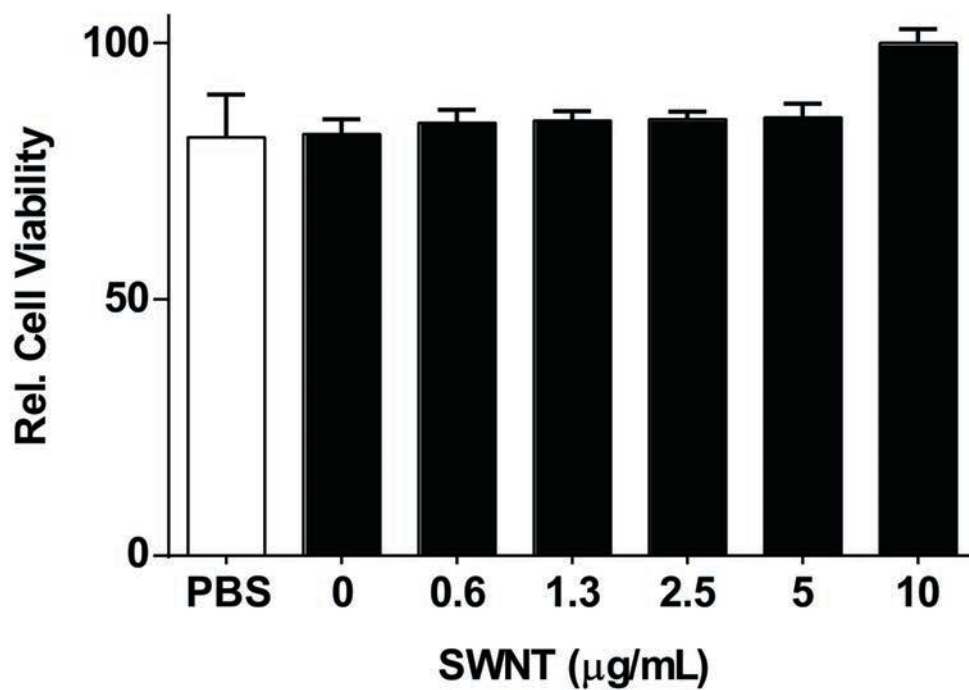
Fig. S5. Primary human endothelial cell (HUVEC) cytotoxicity when incubated with varying concentrations of SBP-M13-SWNTs (n = 4, SWNTs; n = 24, PBS). Error bars denote standard error.

Figure S6.
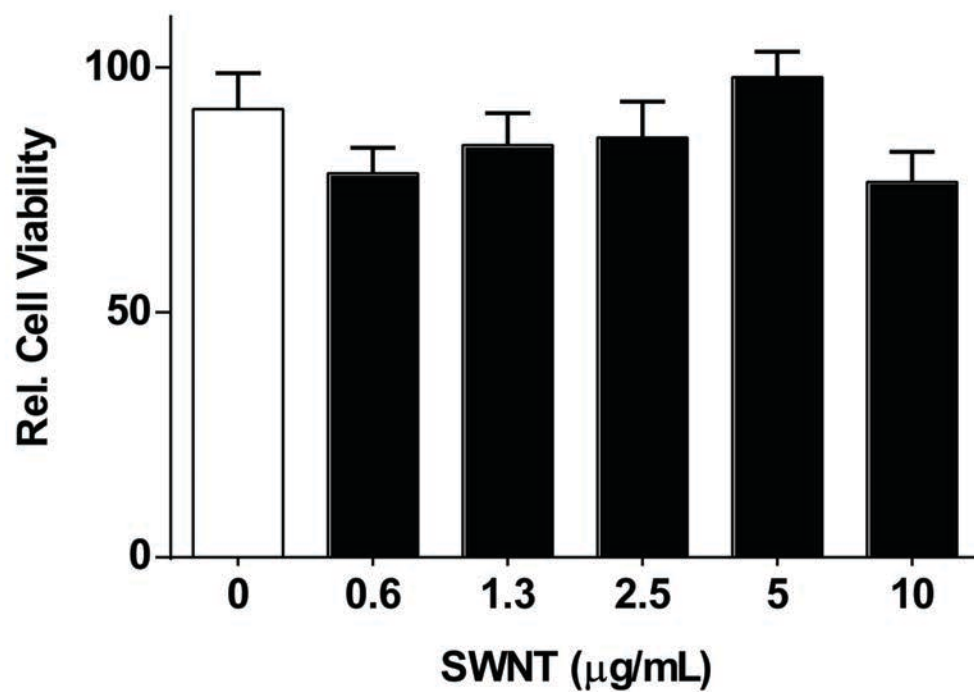
Fig. S6. OVCAR8 viability in presence of SBP-M13-SWNTs. Cells incubated in the presence of

SBP-M13-SWNTs remain viable at [SBP-M13-SWNT] between 0 - 10 ug/mL. Six samples were

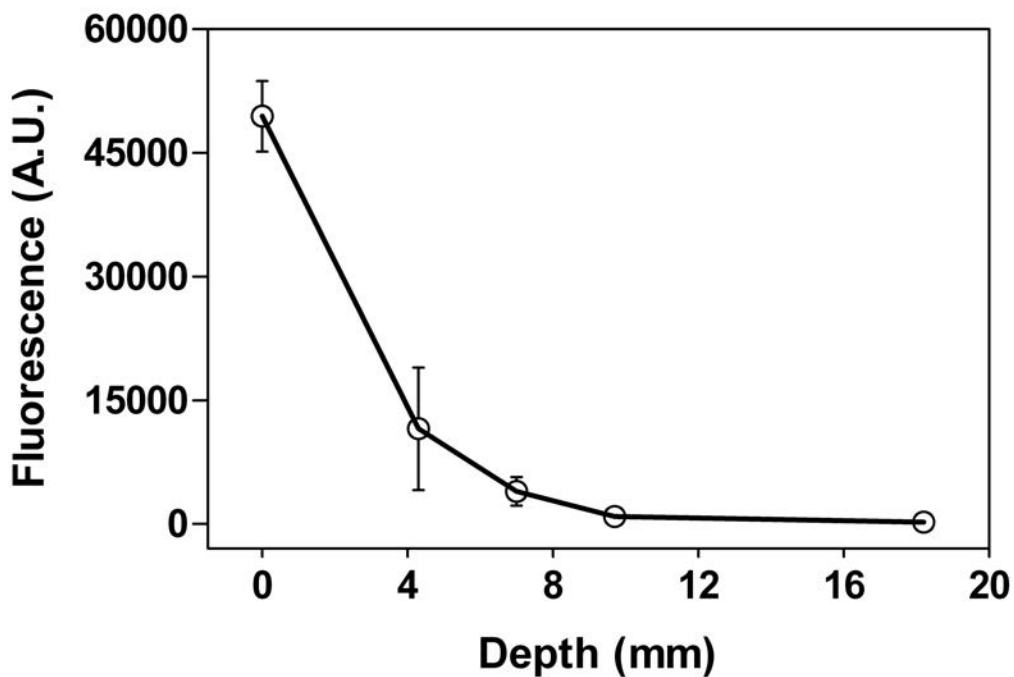run for each experimental condition. Error bars denote standard error (n = 6).

Figure S7.

Fig. S7. Depth of detection of tumors labeled with SBP-M13-SWNTs. Tumors containing SBP-M13-SWNTs were excised from mice into 1 mm diameter fragments and placed within a tissue phantom at varying known depths (0, 4.3, 7.0, 9.7, or 18.2 mm). Samples were imaged using a custom-built fluorescence imager at 0.5 s exposure. Samples were detectable to depths as great as 9.7 to 18.2 mm in the tissue phantom. Five samples were measured per condition. Error bars denote standard deviation (n = 5).
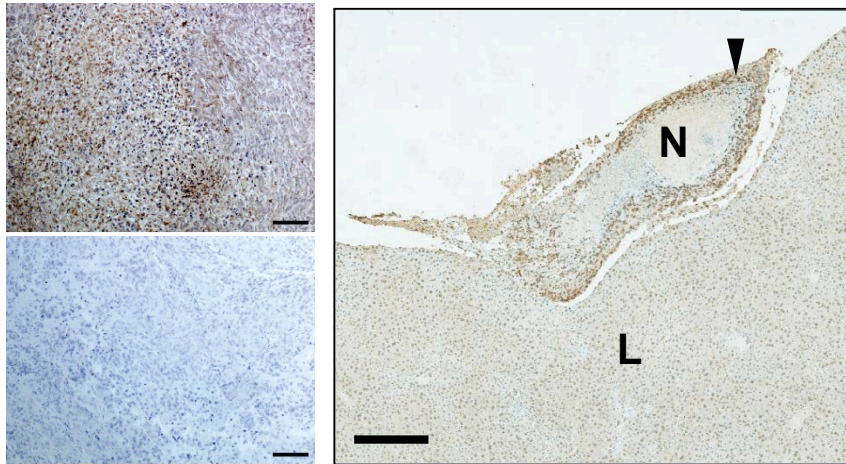
Figure S8.

Fig. S8. SPARC Expression in OVCAR-8 Tumors. OVCAR-8 subcutaneous xenografts (left top; isotype control shown on left bottom) and orthotopic tumors (right) were processed for immunohistochemistry and examined for expression of SPARC. Both subcutaneous and orthotopic OVCAR-8 tumors express SPARC protein. Enhanced SPARC expression observed in the viable tumor rim of the orthotopic nodule (N, expression indicated by black arrow) seeded on liver (L). This is the same nodule analyzed in Figure 2d. Scale bars: 100 μm (left top, bottom), .1 mm (right)
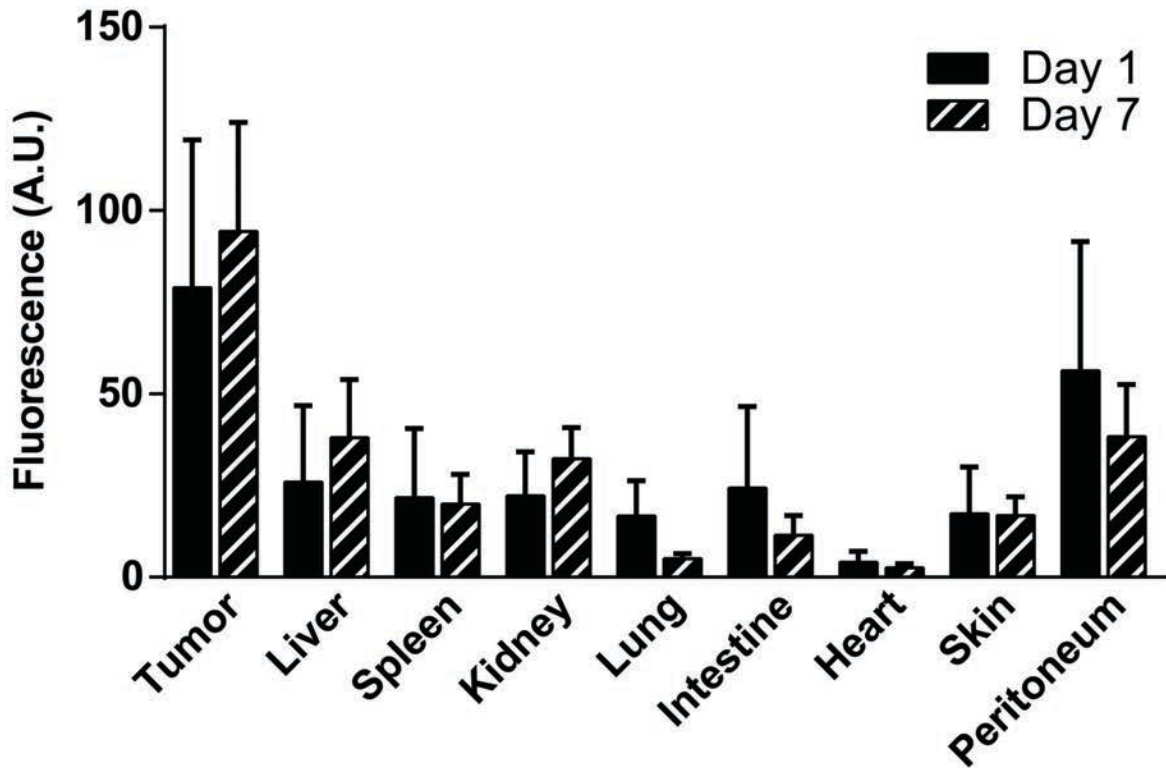
Figure S9.

Fig. S9. Biodistribution of SBP-M13-SWNTs. Biodistribution of intraperitoneally-administered SBP-M13-SWNTs labeled with AF750 at Day 1 post-injection and Day 7 post-injection, as determined by whole tissue fluorescence measurements. Skin and peritoneum were sampled from the injection site region. Data are presented as mean fluorescence intensity (n = 3-5 animals per condition) Error bars denote standard error.
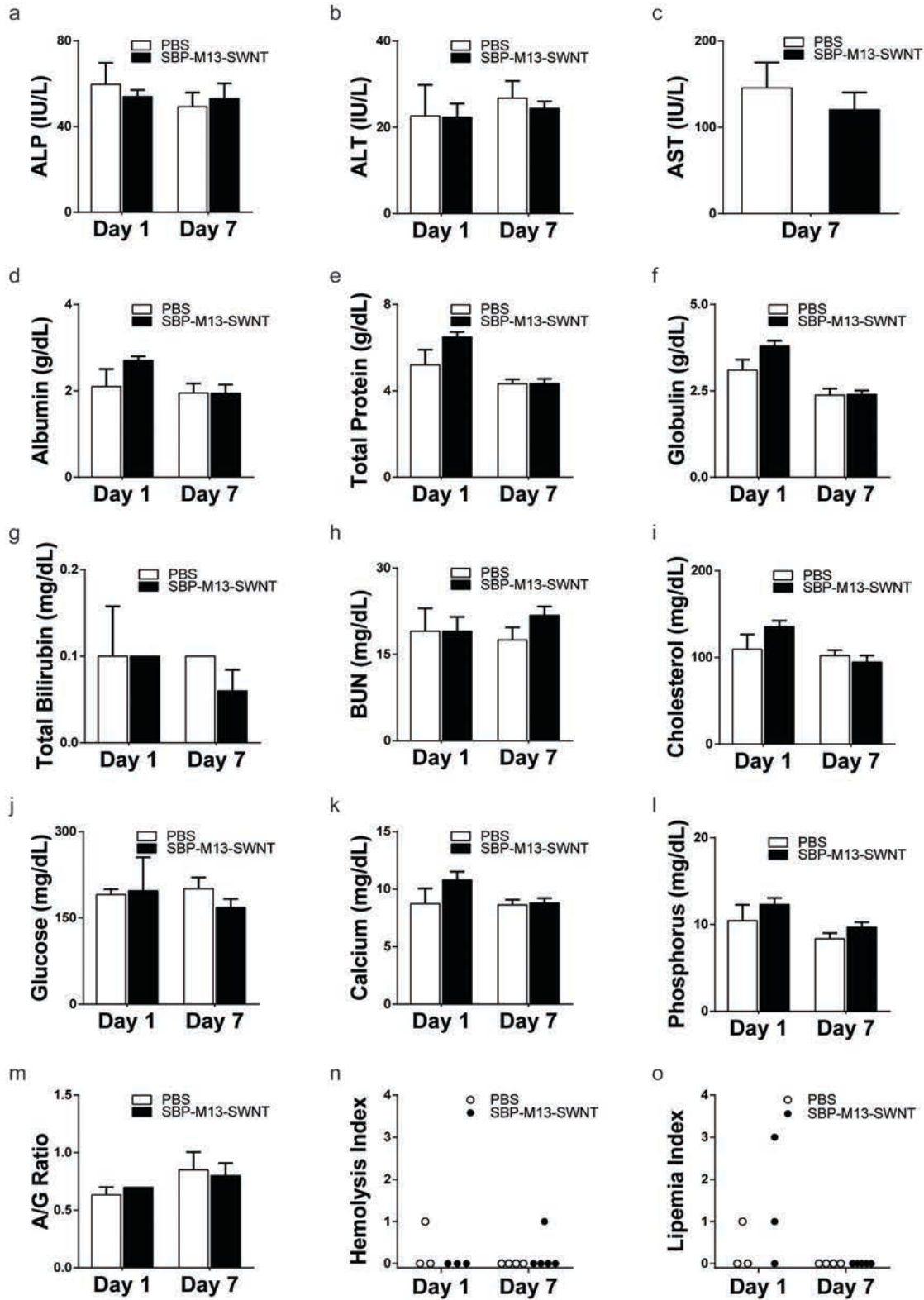
Figure S10.

Fig. S10. Serum chemistry and metabolic profiling. (a-o) Analysis of serum isolated at Day 1 post-injection and Day 7 post-injection from animals administered intraperitoneal SBP-M13-SWNTs to assess for hepatic, renal, metabolic, and hematological acute toxicities. No significant differences between experimental and control cohorts for acute toxicity were detected for all metabolites and time points. (n = 3-5 animals per group, 2-way ANOVA with Sidak's multiple comparisons test) Error bars denote standard error.
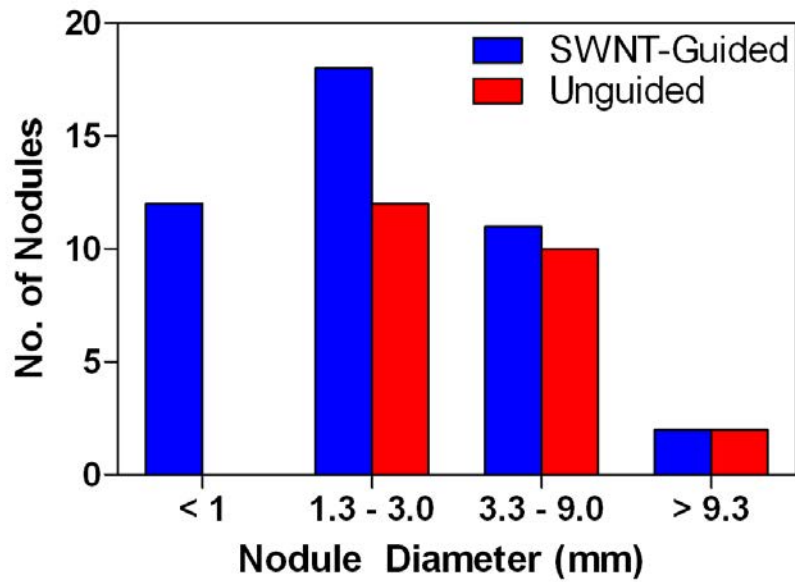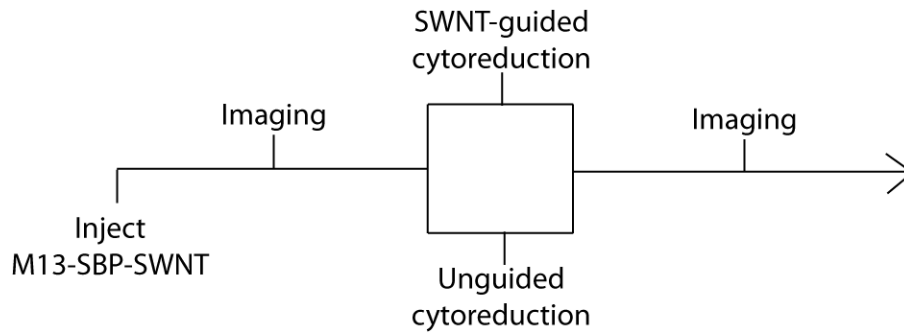
Figure S11.

Fig. S11. Comparison of SWNT-Guided and Unguided Cytoreduction. Tumor-bearing animals were randomized to receive SWNT-guided or unguided cytoreduction. Excised tumors were measured along their maximum diameters prior to tissue fixation. Tumor diameters for each treatment group are plotted as a histogram. (n = 43 nodules, SWNT-guided; n = 24, unguided)

References

1. Yi H*, et al.* (2012) M13 phage-functionalized single-walled carbon nanotubes as nanoprobes for second near-infrared window fluorescence imaging of targeted tumors. *Nano Lett* 12(3):1176-1183.
2. Kelly KA, Waterman P, & Weissleder R (2006) In vivo imaging of molecularly targeted phage. *Neoplasia* 8(12):1011-1018.
3. Ghosh D*, et al.* (2012) M13-templated magnetic nanoparticles for targeted in vivo imaging of prostate cancer. *Nat Nanotechnol* 7(10):677-682.
4. Dang X*, et al.* (2011) Virus-templated self-assembled single-walled carbon nanotubes for highly efficient electron collection in photovoltaic devices. *Nat Nanotechnol* 6(6):377-384.